A giant volcanic island in an early Martian Ocean?

A. Hildenbrand, H. Zeyen, F. Schmidt, S. Bouley, F. Costard, P.Y. Gillot, F.O. Marques, X. Quidelleur

A giant volcanic island in an early Martian Ocean?

A. Hildenbrand[1]*, H. Zeyen[1], F. Schmidt[1], S. Bouley[1], F. Costard[1], P.Y. Gillot[1], F.O. Marques[2], X. Quidelleur[1]

[1] *Université Paris-Saclay, CNRS, GEOPS, Orsay, 91405, France*

[2] *Universidade de Lisboa, Lisboa, Portugal*

*corresponding author: Email: anthony.hildenbrand@universite-paris-saclay.fr

Word count (main text, excluding abstract, references, table and figure captions): 4942

Figure count: 5, equivalent to 1.2 printed pages in total (provided as individual separate files)

Supplementary Figure count: 5 (provided in a separate file)

References: 56

Abstract

Tracking early oceans on Mars has fundamental climatic and exobiological implications but requires unambiguous datable markers. Here we show that the Olympus Mons giant volcano shares morphological similarities with active volcanic islands on Earth where major constructional slope breaks systematically occur at the sea-air transition in response to sharp lava viscosity contrasts. We propose that the upper rim of the 6-km high concentric main escarpment surrounding Olympus Mons most likely formed by lava flowing into liquid water when the edifice was an active volcanic island during the late Noachian - early Hesperian. Similar features on the northern flank of the 1800 km-distant Alba Mons volcano further support an extended early Ocean initially occupying Martian lowlands. Abnormal current shoreline heights imply major surface uplift promoted by internal dynamics during the main phase of development of the Tharsis Bulge at some time during the Hesperian. After ocean retreat, the uplifted shorelines were partly blanketed by late sub-aerial activity during the Amazonian. The newly proposed volcanic shorelines can be dated by radiometric methods, constituting exceptional targets to track early liquid water at key temporal steps and provide valuable insights into the timing and fate of Martian Oceans.

Keywords: *Olympus Mons, Volcanic Island, Basal Escarpment, sea-air transition, Subsidence, Uplift*

1. Introduction

Increasing evidence support the existence of early ocean(s) of liquid water at the surface of Mars until at least 3.0 Ga ago (Schmidt et al., 2022). Where and when such early ocean(s) were has fundamental implications regarding Mars climatic evolution and potential extra-terrestrial life, but remains poorly constrained. In Martian northern plains, two main sets of paleo-shorelines have been attributed to two independent bodies of liquid water that were separated from each other by hundreds of millions of years, between ca 3.8 and 3.0 Ga (e.g. Sholes et al., 2021). Nevertheless, their elevations vary by several kilometres, which may either reflect large fluctuations in ocean(s) level and/or significant ups and downs of the planet surface in response to deformation associated with internal dynamics (e.g. Citron et al., 2018; Broquet and Andrews-Hanna, 2022). Improved knowledge of sea level at key steps of planetary evolution is therefore needed to better constrain ocean(s) reconstructions and elucidate the fate of early liquid water at the surface of Mars. Martian volcanoes constitute potential targets of major interest for such purpose, because (1) their formation under aerial/submarine conditions may have produced distinctive morphologies, and (2) radiometric dating is achievable on most volcanic products, potentially providing key absolute ages in the future. Here we identify a new possible marker of an ancient shoreline, the fossil passage zone of sub-aerial lavas flowing into a liquid ocean, which seems to be well preserved at the upper rim of the Olympus Mons basal escarpment. The apparently excessive height of this new marker can be explained by high-magnitude surface uplift promoted by large-scale mantle upwelling, as shown by new modelling of vertical movements.

Olympus Mons is a more than 20 km-tall shield volcano located on the northwestern slope of the Tharsis rise (Fig. 1). This giant volcanic edifice (>300000 km^2) was most likely formed by protracted hot-spot volcanism above a stationary lithosphere in the absence of plate tectonics. Reported ages for Olympus Mons volcanic activity range from 3.8 Ga to less than 10 Ma (Hiller et al., 1982; Neukum et al., 2004; Werner, 2009; Isherwood et al., 2013). Most of the volcano growth is believed to have taken place before $2.54^{+0.55}_{-0.69}$ Ga (Isherwood et al., 2013), which

comprises the admitted period for a possible early Martian Ocean prior to 3.0 Ga. Olympus Mons exhibits striking morphological features from the centre to the outer parts: (1) The summit area, which includes several nested elliptic depressions formed by vertical caldera collapse (e.g. Mouginis-Mark, 2018); (2) a series of morphological "terraces", which may either mark the edge of successive thick lava flows or centripetal thrusts formed during gravitational spreading of the volcano (Musiol et al., 2016); (3) arcuate cliffs, referred to as the "basal escarpment", which can be traced all around the volcano; (4) a large "aureole" of chaotic deposits, which may represent either debris-avalanches deposits formed by flank collapse processes, highly fragmented lava flows, or late moraine-like glacial deposits (e.g. Lopes et al., 1980; Head et al., 2005); and (5) recent volcano-tectonic features including narrow grabens and vents, which developed in various sectors of the volcano during the late Amazonian (Peters and Christensen, 2017).

The origin of the basal escarpment remains enigmatic. Part of it has been interpreted as a constructional feature possibly influenced by the presence of liquid water (De Blasio, 2012). Yet, the exact relationships between volcano growth and potential water height/depth remain elusive, as the upper tip of most of the escarpment is several kilometres higher than any reported sea level for a past Martian Ocean (e.g. Sholes et al., 2021). Alternatively, the escarpment has been widely interpreted as a series of scarps produced by landslide processes, which truncated the distal flank of the volcano and cumulatively fed the aureole deposits (e.g. Lopes et al., 1980; De Blasio, 2018). However, most of the volcano outline is sub-circular, i.e. concave towards the centre. This seems incompatible with formation of most of the escarpment by lateral slides, which would produce opposite scarp curvature (concave outwards).

2. Morphology of Olympus Mons and characteristics of the escarpments

MOLA topographic data (Smith et al., 1999) allow further identification of striking morphological characteristics at the full scale of Olympus Mons (Fig.1):

- The volcanic edifice is asymmetrical. The western flank covers a wider area than the eastern flank (Fig. 1a), and typically displays lower slopes (Fig. 1b).
- Two main sub-circular basal escarpments are visible in the SE and NW sectors (C1 and C2, Fig. 1a). They can be traced over hundreds of kilometres and are noticeably concave to the centre of the volcano. Both interrupt abruptly the gentle distal flanks of the shield and show relatively steep slopes, with individual values up to 35-40° (Fig. 1b) and average escarpment slopes around 14° and 16° along profiles 2 and 6, respectively (Fig 1c).
- The NW and SE escarpments are ca 6 and 7 km high, respectively, due to a slight westward increase in basement depth. Their upper tips, however, occur at similar elevations, thus supporting the inference of a former presence of a common horizontal free surface all around the volcano.
- Additional concave cliffs can be traced in the southern sector. They appear less prominent, being partly smoothed by late lava fields (Fig. 1).
- In the northern and western sectors, the C2 escarpment is interrupted by convex U-shaped depressions bordered by debris fields typical of flank collapse processes (e.g. Siebert, 1984; Hildenbrand et al., 2018). Other subtle U-shaped scars in the NW and NE sectors were also likely formed by lateral flank destabilization, and later smoothed by volcanic products including a large lava field (Fig. 1 b, c).
- Many other parts of the volcano have been re-surfaced. The basal escarpments, especially, have been deeply modified by smaller-scale landslides, canyon incision, accumulation of piedmont deposits, or cliff concealing by recent lava flows. Nevertheless, these secondary processes did not erase the major morphological characteristics, especially the regional expression of the C1 and C2 prominent cliffs.

3. Comparison with current volcanic ocean islands on Earth

Intra-plate volcanic islands on Earth rise up to 10 km from the oceanic basement and may constitute our best terrestrial analogues to Olympus Mons. Among many examples in various provinces (e.g. Azores, Canary, Cape Verde, Reunion, Hawaii, Galapagos), we selected three islands with contrasted sizes and varied eruptive histories. Both show well-preserved young constructional morphologies, along with older sectors affected by other geological and coastal processes (Fig. 2).

Pico Island (Azores, Atlantic Ocean), the smallest, was formed by successive episodes of growth and repeated destabilization by lateral landslides during the last 200 kyr (Hildenbrand et al., 2012; Costa et al., 2015; Marques et al., 2021). The young Pico Volcano (PV in Fig. 2) is elliptic in plan view. Topographic cross-sections (Fig. 2) show a steep summit area (35°) followed by a gentle regular northern sub-aerial flank (<10°). A sharp break occurs close to the air-sea transition, with a main slope increase by a factor 2, i.e. an angular difference of about 10°. The PV's southern flank is shorter and truncated by a steep U-shape landslide structure yielding an inward-convex coastal embayment.

Fogo Island (Cape Verde, Atlantic), of intermediate size, comprises a main former volcanic edifice that was destroyed by a massive east-directed flank collapse (Day et al., 1999) about 50 ka ago (Marques et al., 2019). The preserved western flank of the former volcano appears sub-circular in plan view, and shows typical constructional profiles (Fig. 2). A sharp morphological break occurs at shore level, with sub-aerial and submarine constructional slopes of ca 10° and 25°, respectively. The still-active Fogo volcano that grew on the landslide scar also shows a short eastern flank with a pronounced slope break at sea level.

The Big Island (Hawaii, Pacific Ocean), by far the largest on Earth, comprises five coalescent shield volcanoes with ages decreasing towards the southeast (Sherrod, et al., 2021). The flanks of the Mauna Loa active volcano (Fig. 2) are cut by several large flank collapse structures partly buried by recent volcanic products (e.g. Moore et al., 1994; Sherrod et al., 2021).

The conspicuous Hilina slump is presently displacing the whole SE flank downwards at rates up to 10 cm/yr (e.g. Morgan et al., 2000; Owen et al., 2000), thus making a significant step (Fig. 2). Topographic profiles in zones not affected by major slides show typical constructional slopes. A marked angular difference of about 13° is observed at the air-sea transition, with average values around 4° and 17° for the sub-aerial and submarine slopes of Mauna Loa, respectively. The Kilauea active volcano developed at the head of the Hilina slump shows a similar constructional slope break at shore level. Deeper steps in the eastern and northern sectors likely witness older shorelines carried down by island subsidence due to loading of the lithosphere during/after the main shield-building phase (e.g. Taylor, 2019, and references herein).

The youngest portions of the three selected volcanic islands exhibit clear constructional main slope breaks at shore level, by up to 15° in magnitude. These can be explained by sharp viscosity contrasts due to differential lava cooling into air or water (Griffiths, 2000) as currently observed at the passage zone between submarine and sub-aerial volcanic series on uplifted oceanic islands, e.g., Santiago in Cape Verde or Santa Maria in the Azores (Marques et al., 2020a,b). In the latter case (Fig. 3), the main constructional slope break coincides with a sudden increase in lava flow dip, from gentle in the sub-aerial part to steeper in the submarine portions, where pillow-lavas and pillow breccias witness fast cooling in the presence of liquid water (Fig. 3). By analogy, the main slope break (ca. 13°) at the upper tips of the C1 and C2 inward concave escarpments surrounding Olympus Mons (Fig. 1) supports contrasted lava viscosity at shore level. This leads us to propose that Olympus Mons was a former volcanic island surrounded by liquid water.

One may argue that alternative processes like lava-ice interactions should be considered, as Martian northern lowlands may have been occupied by a (partially?) frozen ocean during the late Hesperian (Ivanov et al., 2014, 2015). On Earth, lava-ice interactions produce a variety of glacio-volcanic edifices, referred to as “tuyas” (see review in Russell et al., 2014). Flat-topped

tuyas, especially, form as magma rises under a thick ice cap leading to development of a transient lake. As in marine environments, early interactions between hot lavas and melt water sometimes produce subaqueous tephra and/or pillow-lavas, followed by the eruption of sub-aerial lavas once the lake has been drained. As a result, flat-topped "tuya" comprise an upper gentle plateau surrounded by steep slopes, making a significant morphological step like the main slope break around Olympus Mons. Nevertheless, tuya formation is a very local process that typically occurs during a single main eruption, and is therefore an "instantaneous" process at geological timescales. Terrestrial tuyas have small dimensions (few kilometres width, few hundred meters high), and rarely exhibit conical regular morphologies. For these reasons, it seems highly unplausible that the well-behaved slope break observed for hundreds of kilometres around Olympus Mons could have been formed simply by past interactions between a batch of rising magma and a thick frozen ocean.

Lava flowing into a large ocean of (still) liquid water thus remains the most likely scenario to explain both the sub-circular aspect of the main escarpments surrounding Olympus Mons and the conspicuous slope-break with a main angular difference by ca 13°. Conversely, late lava fields (Fig. 1, profile 3) show monotonous and regular slopes typical of terrestrial sub-aerial volcanoes. These low-viscosity lavas most likely partially concealed the escarpment cliffs after water retreat.

4. Ups and downs: Olympus Mons *vs* Martian ocean(s)

The average height of the main escarpments suggests a 6 km-thick column of liquid water initially surrounding the inferred volcanic island. This is more than the average depth of oceans on Earth, and twice the plausible depth for an early Martian ocean ca 3.8 Ga ago (Parker et al., 1993; Sholes et al., 2021). Nevertheless, the escarpment height is not inconsistent with a globally shallow ocean. Massive loading by volcano construction may, indeed, have favoured the fast

development of a peripheral flexural basin, as observed for oceanic lithosphere on Earth (Watts and Zhong, 2000), leading to increasing water column around the growing edifice.

The earliest stages of growth of Olympus Mons remain poorly dated. Ages around 3.8 Ga were reported from in-situ crater counting (HRSC data) near the upper tip of the northwestern basal escarpment (Neukum et al., 2004). These ages have been later discarded (Isherwood et al., 2013), as they were based on only 4 craters of large size (>1 km^2). Additional crater-counting age estimates (Hiller et al., 1982; Isherwood et al., 2013) have been proposed, but these were acquired on indirect, distant markers. An age value of $3.67^{+0.05}_{-0.10}$ Ga (Isherwood et al., 2013) was derived for a "discordant" lava flow exposed 500 km away from the volcano's NE outline. Deviation in the path of the flow from the down-slope direction of the present-day flexural trough is believed to indicate that the flow pre-dates downward lithosphere flexure by main volcano load, and therefore that the dominant growth of Olympus Mons occurred after $3.67^{+0.05}_{-0.10}$ Ga (Isherwood et al., 2013). However, this flow is located tens of kilometers away from the main though rim, and its sinuous path might just reflect channeling of the lava in a local topography either before, during, or after lithosphere flexure. On the other hand, the northern aureole deposits have been attributed to late landslide processes post-dating Olympus Mons main building-phase. Crater-counting in the northern aureole yielded initial age estimates between 3.68 Ga and 3.51 Ga (Hiller et al;, 1982). More recent estimates (Isherwood et al., 2013) range between $3.47^{+0.07}_{-0.16}$ Ga and $0.98^{+0.51}_{-0..61}$ Ga, with a preferred value of $2.54^{+0.55}_{-0.69}$ Ga, i.e up to 2.99 Ga when uncertainties are accounted for. Therefore, the bulk of the volcano most likely grew up prior to 3.0 Ga, and possibly as early as 3.7-3.6 Ga ago if we consider the oldest ages reported for both the basal escarpment and the northern aureole deposits (Hiller et al., 1982; Neukum et al., 2004; Werner, 2009; Isherwood et al., 2013).

Noticeably, the northern aureole was partly fed by the recent slide interrupting the C2 concave cliff here interpreted as a former shoreline (Fig. 1). Olympus Mons thus most likely was

already a large and thick volcanic island with dimensions comparable to present-day when the slide occurred. Significant flexural subsidence and basin deepening by dominant volcano load may thus have taken place during either the late Noachian or early Hesperian (Fig. 4a, b), which is significantly earlier than previously proposed (Isherwood et al., 2013).

Figure S1 shows our new modelling results for downward loading of the lithosphere by a former edifice with variable thicknesses (model description in Appendix A). An initial volcano height of 15-20 km is sufficient to produce a 1300 km-wide flexural basin (Fig. S2) and locally increase global ocean water depth by a few kilometres around the volcano. Nevertheless, the basal escarpment upper tips stand more than 6.5 km higher than the values commonly reported for early shorelines on Mars (Arabia level, 3.7 Ga, elevation between -3.6 km (Sholes et al., 2021) and -1.6 km (Parker et al., 1993)), and about 10 km higher than the youngest ones (Deuteronilus level, ca 3.0 Ga, mean elevation around - 4 km (Sholes et al., 2021; Schmidt et al., 2022)). Therefore, generalized island uplift by at least 6 - 7 km is needed to explain the present position of the main slope break.

Dynamic swelling (plume load) associated with main development of the Tharsis Rise during the early to middle Hesperian (Bouley et al., 2018) could have promoted surface uplift by several hundreds of meters to kilometres (Fig. 4c), as recorded by some oceanic volcanoes on Earth (e.g. Moore et al., 1999; Zhong and Watts, 2002; Hildenbrand et al., 2003; Marques et al., 2020a,b). Dynamic uplift is here tested considering upward impact of the Martian lithosphere by an elliptical mantle anomaly centered underneath OM (Fig. S3). A plume with a 1000 km radius and 650 km thickness, an excess temperature of 300 °C and thus a buoyancy of 1% with respect to ambient mantle can produce a swell exceeding 6 km. Possible effects of magma underplating are further tested considering low-density material ponded underneath the Martian crust (Fig. S4). A 10 km-thick body with a geometry mirroring volcano topography could produce additional surface rise of more than 2 km. Other mechanisms such as multiple sill intrusions during recent volcanic activity (Fig. 4d) or late isostatic readjustment after melting of a thick icesheet could

also contribute to further edifice uplift but may be rather limited, as inferred from glacial isostatic adjustment on Earth (e.g. Steffen and Wu, 2011).

5. A scenario applicable to other Martian volcanoes?

Alba Mons appears a good candidate to further track the presence of past liquid water on Mars and evaluate vertical movements at regional scales. Alba Mons straddles the northwestern edge of the Tharsis rise, 1800 km North of Olympus Mons (Fig. 5). Estimated ages from crater counting suggest dominant volcano construction between 3.6 Ga and 3.2 Ga (Ivanov and Head, 2006), which partly overlaps the updated time pace for a possible Martian ocean (Schmidt et al., 2022) and the currently inferred age for the development of the Tharsis bulge (Bouley et al., 2016; Citron et al., 2017; Broquet and Andrews-Hanna, 2022). The Alba Mons asymmetric shield-volcano is outlined by arcuate volcano-tectonic structures and sharp N-S lineaments associated with late-stage faulting (e.g. Ivanov and Head, 2006; Leone et al., 2021).

While most of the edifice features very gentle regular flanks, the northern edge shows a clear slope break (Fig. 5). The observed angular difference (<2°) is much smaller than in the case of Olympus Mons and terrestrial cases. This possibly indicates lower viscosity of the magma erupted at Alba Mons, or partial concealing/smoothing of an initial steeper slope break by late lavas, as suspected for some sectors of Olympus Mons (Figure 1, profile 7). Nevertheless, the relative jump in slope by a factor 2 across the northern flank of Alba Mons is still significant, and may witness a former passage zone from sub-aerial to submarine environments, as proposed for the C1 and C2 cliffs around Olympus Mons. The smaller height of Alba Mons relatively steep lower flank (<5 km) may reflect (a) the peculiar position of the edifice at the margin of an ocean basin, inducing a shallower water depth, (b) reduced flexural subsidence due to a shorter volcanic edifice (<8 km), (c) a younger and globally shallower ocean during the early Hesperian, and (d)

emplacement of the volcanic edifice during/after initiation of the uplift associated with the Tharsis Rise.

Despite significant differences, Alba Mons and Olympus Mons overall share common morphological characteristics, which support two main stages of evolution in the northwest Tharsis region: (1) early volcanic construction in the presence of liquid water in the northern plains, and (2) significant regional uplift during early-middle Hesperian, eventually followed by late sub-aerial volcanism after water retreat.

6. Broader implications

The new markers of sea level here proposed stand much higher than elevated shorelines previously identified around the Tharsis Rise (longitudes between -150°E and -120°E), supporting significant additional uplift. From our new modelling, a buoyant mantle plume with a 1000 km radius centered underneath Olympus would produce no significant surface uplift at Alba Mons. A larger plume (2000 km radius) impacting the lithosphere below the central part of the Tharsis bulge ca 3.5 Ga ago could have produced comparable large magnitude surface uplift of both volcanoes. However, such large-scale doming would cause differential uplift between the western and eastern parts of Olympus Mons, which is not supported by the comparable elevation of the C1 and C2 upper escarpment rims. Alternatively, both volcanoes may have experienced regional uplift in response to upward loading by distinct plumes of moderate sizes. Such features may be connected to a wider deep mantle anomaly under the Tharsis region, as proposed for the South Pacific Superswell on Earth, where plumelets separated by hundreds of km rise periodically from a super-plume blocked at depth (Courtillot et al., 2003; Bonneville et al., 2006). Rejuvenated volcanism (<3 Ga) on Olympus Mons and at the scale of the whole Tharsis dome (e.g. Leone et al., 2021) further suggests extended and protracted partial melting, supporting large-scale mantle upwelling during the late Hesperian and part of the Amazonian. According to

a recent study (Broquet and Andrews-Hanna, 2022), a currently still-active large plume head (nominal radius around 2000 km) could account for a surface uplift of about 1 km for the Elysium Planitia region during the late Amazonian, further supporting the protracted influence of deep Martian geodynamics as a main carrier of surface deformation.

7. Conclusions

Conspicuous slope breaks at the top of the main basal escarpment surrounding Olympus Mons are here interpreted as paleo-shorelines around a former volcanic island. Similar features at Alba Mons further support the existence of an early ocean occupying the northern plains of Mars along the NW edge of the Tharsis region. The proposed shorelines stand much higher than previously reported late Noachian sea levels, suggesting later high-magnitude regional uplift in response to deep internal forcing. Plume buoyancy leading to upward deformation of the Martian lithosphere associated with the main development of the Tharsis Rise could adequately explain such large-scale vertical movements followed by widespread late sub-aerial volcanism in the region.

Improved age determination is needed to better constrain the timing for ocean stability and the dynamics of large vertical movements. Volcanic units involved in the slope breaks at Olympus Mons constitute exceptional targets for such a purpose. Recent analytical advances in in-situ K-Ar radiometric dating (e.g Cho and Cohen, 2018; Cattani et al., 2019; Cohen et al., 2021) presently allow age measurement on Mars-like volcanic materials with relative precision of only a few percent. Future spacecrafts dedicated to sample return and/or rover equipped for in-situ dating on selected sites of Olympus Mons constitute a promising line of research for the future, which can have significant impact regarding the longevity of oceans and the potential fate of early life on Mars.

Appendix A: Methods

Shaded-relief maps, slope maps, and topographic profiles of Olympus and Alba Mons have been generated from the MOLA global digital elevation model[16] with a spatial resolution of 200 m. The size of each DEM cell is very small compared to the actual size of both volcanoes (> 300000 km^2 each), enabling a fine assessment of the main morphological characteristics of both edifices. Morphological analyses of the three volcanic islands here considered have been achieved from DEMs merging topographic and bathymetric data. Source of the data for Pico is from the EMODNET European open-access database. Public data for Hawaii (http://www.soest.hawaii.edu/hmrg/multibeam/bathymetry.php) is available from the School of Ocean and Earth Science and Technology (SOEST, University of Hawaii). Data for Fogo (Le Bas et al., 2007) have been made available to us by T. Le Bas (Univ. of Southampton, UK).

Modelling the deformation induced by either volcano load, upward plume load, and magma underplating has been achieved considering a purely elastic behaviour. Proper estimation of the lithosphere elastic thickness at the time of loading is essential for such purpose. Seismic data acquired recently during the insight mission in Elysium Planitia about 5 000 km away from Olympus Mons have shown the presence of deep reflectors interpreted as evidence for current thickness of 500 km for the Martian lithosphere (Kahn et al., 2021). However, a much thinner lithosphere thickness is expected at the time of loading here considered, mostly between ca 3.8 and 3.0 Ga ago.

Bending of an elastic plate depends on the acting forces and the elastic parameters of the plate. For a two-dimensional periodic loading and laterally constant elastic parameters, the following formula describes bending (Turcotte and Schubert, 2002):

$$w(x) = \frac{F_l}{F_r + D\left(\frac{2\pi}{\lambda}\right)^4} \quad \text{(eq. 1)}$$

where w [m] is the deformation of the plate in the (vertical) direction of the applied force, F_l = ρ_r*g*h [N/m^2] is the loading pressure with ρ_r the effective density of the restoring mass and h the height of the load, F_r [N/m^3] is the restoring pressure per unit length of deformation w, D = $ET_e^3/[12(1-\nu^2)]$ is the flexural rigidity [Nm] with E [Pa] Young's modulus, ν Poisson's ratio and T_e [m] the equivalent elastic thickness of the deformed plate. λ [m] is the wavelength of the periodic load, the load having thus the form of $F_l = \rho_l * g * h_0 * \sin(2\pi/\lambda * x)$ where ρ_l [kg/m^3] is the effective density of the load, g [m/s^2] the gravity acceleration and h_o [m] the amplitude of load height (topography or plume thickness). The actual distribution of the forces is evidently not periodic, but it is possible to apply eq. 1 to the spectral components of the force distribution. Thus, topography and plume profiles are analysed using Fast Fourier Transform, each coefficient of the resulting spectrum is multiplied by eq. 1 using the wavelength corresponding the respective coefficient and the filtered spectrum is then transformed back into real space.

For a topographic load, the density ρ_l is the density of the material building the topography whereas the effective density of the restoring mass is $\rho_r = \rho_m - \rho_f$, ρ_m being the density of the mantle and ρ_f the density if the infill of the flexural basin. Since we suppose that the basin was filled with water, we use for ρ_f 1000 kg/m^3. For a plume load, the effective density of the load is the density difference between the hot plume and the surrounding mantle: $\rho_l = \rho_m - \rho_p$. ρ_p depends on the temperature difference ΔT [K]: $\rho_p = \rho_m * (1 - k\Delta T)$, k [1/K] being the thermal expansion coefficient, taken as $3.5*10^{-5}$ K^{-1} (e.g. Afonso et al., 2005 for terrestrial mantle). The effective density is thus $\rho_l = -\rho_m * k\Delta T$. For the restoring force, ρ_r is the density of the crust ρ_c for which we take the same density as for the volcanic material.

In the case of Olympus Mons, the values used for the calculations are summarized in Table 1. They were mostly taken from Belleguic et al. (2005). This model scales with the model from Broquet and Andrews-Hanna (2022). Figure S1 shows results for the calculation of

topography resulting from initial volcanism on a plate of variable equivalent elastic thickness (EET). The thickness of deposited volcanic material was adjusted for each tested EET such that the break in slope is located at sea level (defined as 0 m topography). From a point of view of topography of the main volcanic building, EETs from 30 to 150 km are possible if loading has thicknesses between 40 and 18 km respectively. However, the different models are clearly distinguished by the distance of the bulge from the volcanic centre, which varies from 400 to 1000 km. Fig. A2 shows that the bulge visible on the topographic map of OM has a diameter of about 1300 km. An EET of 80 to 100 km with an initial load of about 20 km thickness is thus the most probable scenario during the initial build-up of OM (see Supplementary Figure 3). The EET here obtained is consistent with a value of 83 km previously reported (Taylor et al., 2020) for the elastic thickness of the lithosphere near Olympus Mons.

In order to explain the rise of the break in slope to its actual altitude of about 7 km, we tested different plume models. The topography resulting from adding the effect of a plume with a thickness of 650 km and a temperature difference of 300 K to the initial deformation gave the best result and is shown in Fig. A3. Due to the large width of this plume (radius of 1000 km), its topographic effect is similar for all tested EET and the maximum topography reaches 15 to 17 km. Since the buoyancy is the product of thickness and density contrast, a thinner plume with higher temperature or a thicker one with smaller temperature would give the same results.

Figure S4 shows details of the model and resulting crustal deformation due to different mechanisms (topographic load, underplating, plume) as well as their effect on resulting surface topography for the model with an EET of 80 km. For topographic load and underplating, the sum of resulting surface topography and crustal deformation (taken positive downwards) equals the thickness of the load. For the plume, crustal deformation equals surface topography. The effects vary linearly with the height of each mechanism allowing thus to estimate topography for other load values.

Our modeling approach was further applied to the case of Big Island (Hawaii) as a test. A full investigation with different sets of parameters has been already achieved by others (e.g., Watts and Zhong, 2000; Zhong and Watts, 2002, 2013) and is beyond the scope of the present study. We simply considered here a set of realistic parameters: a topographic load of 13-14 km, an EET of 30 km, crustal underplating of 40 %, crustal density of 2.8 kg/m^3, asthenosphere density of 3.2 kg/m^3, plume excess-temperature of 200°C, plume radius of 250 km, and plume thickness of 200 km. The predicted surface topography (Fig. S5) is overall consistent with the observed topography. Downward lithospheric flexure by volcano load produces an extended basin about 2-3 km deeper than the present topographic surface of the seafloor along the Hawaiian Deep. However, the latter comprises a >2 km-thick sedimentary sequence that gradually filled the basin during main island evolution (e.g. Moore et al., 1994, and references herein). Therefore, modeled basin depth is consistent with the actual depth of the basement (under the sediments), which confirms that our numeric approach reasonably predicts first-order basement deformation.

References

Afonso, J. C., Ranalli, G., Fernàndez, M., 2005. Thermal expansivity and elastic properties of the lithospheric mantle: results from mineral physics of composites. *Phys. Earth Planet. Int.* **149** (3-4): 279-306, doi: 10.1016/j.pepi.2004.10.003.

Belleguic, V., Lognonné, P., Wieczorek, M., 2005. Constraints on the Martian lithosphere from gravity and topography data. *J. Geophys. Res.* **110** (E11), doi: 10.1029/2005JE002437.

Bonneville, A., Dosso, L., Hildenbrand, A., 2006. Temporal evolution of the south-Pacific superplume activity: new data from the Cook-Australes volcanic chain. *Earth Planet. Sci. Lett.*, **244** (1-2), 251-269. https://doi.org/10.1016/j.epsl.2005.12.037

Bouley, S., et al., 2016. Late Tharsis formation and implications for early Mars. *Nature* **531**, 344–347. https://doi.org/10.1038/nature17171

Bouley, S., Baratoux., D., Paulien, N., Missenard, Y., Saint-Bezar, B., 2018. The revised tectonic history of Tharsis. *Earth Planet. Sci. Lett.* **488**, 126-133. https://doi.org/10.1016/j.epsl.2018.02.019

Broquet, A., Andrews-Hanna, J.C., 2022. Geophysical evidence for an active mantle plume underneath Elysium Planitia on Mars. *Nat Astron*, https://doi.org/10.1038/s41550-022-01836-3

Cattani, F. *et al.*, 2019. In-situ K-Ar dating on Mars based on UV-Laser ablation coupled with a LIBS-QMS system: Development, calibration and application of the KArMars instrument. *Chem. Geol.* **506**, 1-16. https://doi.org/10.1016/j.chemgeo.2018.12.010

Cho, Y., Cohen, B. A., 2018. Dating igneous rocks using the Potassium–Argon Laser Experiment (KArLE) instrument: A case study for ~380 Ma basaltic rocks. *Rapid Communications in Mass Spectrometry* **32** (20), 1755-1765. https://doi.org/10.1002/rcm.8214

Citron, R., Manga, M., Hemingway, D., 2018. Timing of oceans on Mars from shoreline deformation. *Nature* **555**, 643–646. https://doi.org/10.1038/nature26144.

Cohen, B.A. *et al*., 2021. In Situ Geochronology for the Next Decade: Mission Designs for the Moon, Mars, and Vesta. *Planet. Sci. J.* **2,** 145. DOI 10.3847/PSJ/abedbf

Costa, A.C.G., Hildenbrand, A., Marques, F.O., Sibrant, A.L.R., Santos de Campos, A., 2015. Catastrophic flank collapses and slumping in Pico Island during the last 130 kyr (Pico-Faial ridge, Azores Triple Junction). *J. Volcanol. Geotherm. Res.* **302**, 33-46. https://doi.org/10.1016/j.jvolgeores.2015.06.008

Courtillot, V., Davaille, A., Besse, J., Stock, J., 2003. Three distinct types of hotspots in the Earth's mantle. *Earth Planet. Sci. Lett.* **205**, 295-308. https://doi.org/10.1016/S0012-821X(02)01048-8

Day, S.J., Heleno da Silva, S.I.N., Fonseca, J.F.B.D., 1999. A past giant lateral collapse and present-day flank instability of Fogo, Cape Verde Islands. *J. Volcanol. Geotherm. Res.* **94** (1–4), 191-218. https://doi.org/10.1016/S0377-0273(99)00103-1

De Blasio, F.V., 2012. Conceptual model for the origin of Olympus Mons cliffs, Mars: an essential influence of water? *Planetary and Space Science* **69**, 105-110. https://doi.org/10.1016/j.pss.2012.04.005

De Blasio, F.B., 2018. The pristine shape of Olympus Mons on Mars and the subaqueous origin of its aureole deposits. *Icarus* **302**, 44-61. https://doi.org/10.1016/j.icarus.2017.11.003

Griffiths, R. W., 2000. The dynamics of lava flows. *Annual review of fluid mechanics* **32** (1), 477-518. https://doi.org/10.1146/annurev.fluid.32.1.477

Head, J. et al., 2005. Tropical to mid-latitude snow and ice accumulation, flow and glaciation on Mars. *Nature* **434,** 346–351. https://doi.org/10.1038/nature03359

Hildenbrand, A., Gillot, P.Y., Soler, V., and Lahitte, P., 2003. Evidence for a persistent uplifting of La Palma (Canary Islands) inferred from morphological and radiometric data. *Earth Planet. Sci. Lett.* **210**, 277-289. https://doi.org/10.1016/S0012-821X(03)00133-X

Hildenbrand, A., Marques, F.O., Catalão, Catita, C.M.S., Costa, A.C.G. , 2012. Large-scale active slump of the SE flank of Pico Island (Azores). *Geology* **40**, 939-942. https://doi.org/10.1130/G33303.1

Hildenbrand, A., Marques, F.O., Catalão, J., 2018. Large-scale mass wasting on small volcanic islands revealed by the study of Flores Island (Azores). *Nature Sci. Rep.* **8** (1), 13898. https://doi.org/10.1038/s41598-018-32253-0

Hiller, K.H., Janle, P., Neukum, G.P.O., Guest, J.E., Lopes, R.M.C., 1982. Mars : Stratigraphy and gravimetry of Olympus Mons and its aureole. *J. Geophys. Res.* **87** (B12), 9905-9915. https://doi.org/10.1029/JB087iB12p09905

Isherwood, R. J., Jozwiak, L. M., Jansen, J. C., Andrews-Hanna, J. C., 2013. The volcanic history of Olympus Mons from paleo-topography and flexural modeling. Earth Planet. Sci. Lett., 363, 88-96. https://doi.org/10.1016/j.epsl.2012.12.020

Ivanov, M.A., Head, J.W., 2006. Alba Patera, Mars: Topography, structure, and evolution of a unique late Hesperian–early Amazonian shield volcano. *J. Geophys. Res.* **111**, E09003. https://doi.org/10.1029/2005JE002469

Ivanov, M.A., Hiesinger, H., Erkeling, G., Reiss, D., 2014. Mud volcanism and morphology of impact craters in Utopia Planitia on Mars: Evidence for the ancient ocean. Icarus 228, 121-140. https://doi.org/10.1016/j.icarus.2013.09.018

Ivanov, M.A., Hiesinger, H., Erkeling, G., Reiss, D., 2015. Evidence for large reservoirs of water/mud in Utopia and Acidalia Planitiae on Mars. Icarus 248, 383-391. https:// doi.org/10.1016/j.icarus.2014.11.013

Kahn et al., 2021. Upper mantle structure of Mars from InSight seismic data. *Science* **373** (6553) :434-438. doi: 10.1126/science.abf2966

Le Bas, T.P., Masson, D.G., Holtom, R.T., Grevemeyer, I., 2007. Slope Failures Of The Flanks Of The Southern Cape Verde Islands. In: Lykousis, V., Sakellariou, D., Locat, J. (eds)

Submarine Mass Movements and Their Consequences. Advances in Natural and Technological Hazards Research, vol **27**. Springer, Dordrecht. https://doi.org/10.1007/978-1-4020-6512-5_35.

Leone, G., Grosse, P., Ahrens, C., Gasparri, D., 2021. Geomorphological and morphometric characteristics of the volcanic edifices along a volcanic alignment of Tharsis on Mars. *Geomorphology* **414**, 108385. https://doi.org/10.1016/j.geomorph.2022.108385

Lopes, R.M.C., Guest, J.E., Wilson, C.J., 1980. Origin of the Olympus Mons aureole and perimeter scarp. *Moon and the Planets* **22,** 221–234. https://doi.org/10.1007/BF00898433.

Marques, F.O., Hildenbrand, A., Victoria, S.S., Cunha, C., Dias, P., 2019. Caldera or flank collapse in the Fogo volcano? What age? Consequences for risk assessment in volcanic islands. *J. Volcanol. Geotherm. Res.* **388**, 106686. https://doi.org/10.1016/j.jvolgeores.2019.106686

Marques, F. O., Hildenbrand, A., Zeyen, H., Cunha, C., Victória, S. S., 2020a. The complex vertical motion of intraplate oceanic islands assessed in Santiago Island, Cape Verde. *Geochem. Geophys. Geosyst.* **21**, e2019GC008754. https://doi.org/10.1029/2019GC008754

Marques, F.O., Hildenbrand, A., Costa, A.C.G. *et al,* 2020b. The evolution of Santa Maria Island in the context of the Azores Triple Junction. *Bull Volcanol* **82**, 39. https://doi.org/10.1007/s00445-020-01378-4

Marques, F.O. et al., 2021. The shaping of a volcanic ridge in a tectonically active setting: The Pico-Faial Ridge in the Azores Triple Junction. *Geomorphology* **378**, 107612. https://doi.org/10.1016/j.geomorph.2021.107612

508 Moore, J. G., Normak, W.R., Holcomb, R.T., 1994. Giant Hawaiian Landslides. Annu. Rev.
509 Earth Planet. Sci. **22** (1), 119-144. https://doi.org/10.1146/annurev.ea.22.050194.001003

510 Moore, W.B., Schubert, G., Tackley, P.J., 1999. The role of rheology in lithospheric thinning by
511 mantle plumes. *Geophys. Res. Lett.* **26**, 1073-1076. https://doi.org/10.1029/1999GL900137

512 Morgan, J.K., Moore, G.F., Hills, D.J., and Leslie, S., 2000, Overthrusting and sediment
513 accretion along Kilauea's mobile south flank, Hawaii: Evidence for volcanic spreading from
514 marine seismic reflection. *Geology* **28**, 667–670. https://doi.org/10.1130/0091-
515 7613(2000)28<667:OASAAK>2.0.CO;2

516 Mouginis-Mark, P., 2018. Olympus Mons volcano, Mars: A photogeologic view and new
517 insights. *Geochemistry* **78** (4), 397-431. https://doi.org/10.1016/j.chemer.2017.11.006

518 Musiol, S. et al., 2016. Lithospheric flexure and gravity spreading of Olympus Mons volcano,
519 Mars. *J. Geophys. Res. Planets* **121** (3), 255–272. https://doi. org/10.1002/2015JE004896

520 Neukum, G. et al., 2004. Recent and episodic volcanic and glacial activity on Mars revealed by
521 the High Resolution Stereo Camera. *Nature* **432**, 971-979.
522 https://doi.org/10.1038/nature03231

523 Owen, S. et al., 2000. Rapid deformation of Kilauea volcano: global positioning system
524 measurements between 1990 and 1996: *J. Geophys. Res.* **105**, 18983–18998,
525 https://doi.org/10.1029/2000JB900109

526 Parker, T. J., Gorsline, D. S., Saunders, R. S., Pieri, D. C., Schneeberger, D. M. (1993). Coastal
527 geomorphology of the Martian northern plains. *J. Geophys. Res.* ***98*** (E6), 11061–11078.
528 https://doi.org/10.1029/93JE00618

Peters, S.I., Christensen, P.R., 2017. Flank vents and graben as indicators of Late Amazonian volcanotectonic activity on Olympus Mons. *J. Geophys. Res. (Planets)* **122**(3), 501-523, https://doi.org/10.1002/2016JE005108

Russell, J.K., Edwards, B.R., Porritt, L., Ryane, C., 2014. Tuyas: a descriptive genetic classification. Quat. Sci. Rev. 87, 70-81. https://doi.org/10.1016/j.quascirev.2014.01.001

Schmidt, F. et al., 2022. Circumpolar ocean stability on Mars 3 Gy ago. *PNAS* **119** (4) e2112930118. https://doi.org/10.1073/pnas.2112930118

Sherrod, D.R., Sinton, J.M., Watkins, S.E., and Brunt, K.M., 2021. Geologic map of the State of Hawai‘i: *U.S. Geol. Surv. Scientific Investigations Map* **3143**, pamphlet 72 p., 5 sheets, scales 1:100,000 and 1:250,000, https://doi.org/10.3133/sim3143

Sholes, S. F., Dickeson, Z. I., Montgomery, D. R., Catling, D. C., 2021. Where are Mars' hypothesized ocean shorelines? Large lateral and topographic offsets between different versions of paleoshoreline maps. *J. Geophys. Res. (Planets)* **126**, e2020JE006486. https://doi.org/10.1029/2020JE006486

Siebert, L., 1984. Large volcanic debris avalanches: characteristics of source areas, deposits, and associated eruptions. *J. Volcanol. Geotherm. Res.* **22**(3-4), 163-197. https://doi.org/10.1016/0377-0273(84)90002-7

Smith, D. et al., 1999. The global topography of Mars and implications for surface evolution. *Science* **284** (5419), 1495–1503. https://www.science.org/doi/10.1126/science.284.5419.1495

Steffen, H., Wu, P., 2011. Glacial isostatic adjustment in Fennoscandia—a review of data and modeling. *J. Geodyn.* **52** (3-4), 169-204. https://doi.org/10.1016/j.jog.2011.03.002

Taylor, B., 2019. Shoreline slope breaks revise understanding of Hawaiian shield volcanoes evolution. Geochemistry, Geophysics, Geosystems, 20, 4025–4045. https://doi.org/10.1029/2019GC008436

Taylor, N.C., Johnson, J.H., Herd, R.A., Regan, C.E., 2020. What can Olympus Mons tell us about the Martian lithosphere? *J. Volcanol. Geotherm. Res*. **402**, 106981. https://doi.org/10.1016/j.jvolgeores.2020.106981

Turcotte, D., Schubert, G., 2002. *Geodynamics* (2nd ed.). Cambridge: Cambridge University Press, 456 p., doi:10.1017/CBO9780511807442

Watts, A. B., Zhong, S., 2000. Observations of flexure and the rheology of oceanic lithosphere. *Geophys. J. Int.* **142** (3), 855-875. https://doi.org/10.1046/j.1365-246x.2000.00189.x

Werner, S., 2009. The global martian volcanic evolutionary history. *Icarus* **201**, 44-68. https://doi.org/10.1016/j.icarus.2008.12.019

Zhong, S., Watts, 2002. Constraints on the dynamics of mantle plumes from uplift of the Hawaiian Islands. *Earth Planet. Sci. Lett.* **203**, 105-116. https://doi.org/10.1016/S0012-821X(02)00845-2

Zhong, S., Watts, 2013. Lithospheric deformation induced by loading of the Hawaiian Islands and its implications for mantle rheology. J. Geophys. Res. 118 (11), 6025-6048. https://doi.org/10.1002/2013JB010408

Authors contribution

AH conceptualized the study, performed the geomorphological analyses, and wrote the first draft. HZ conducted the numerical modelling of plate deformation. FS and SB took of care of the aspects related to the age and extent of Martian Oceans and formation of the Tharsis Bulge. All authors contributed to scientific discussions/inputs, and drafting of the article.

Acknowledgments

We acknowledge two anonymous reviewers for their insightful remarks, which helped to significantly improve the manuscript. This is LGMT contribution 180.

581 **Table captions**

582 Table 1: Parameters used in the calculations of elastic plate deformation

583

584 **Figure captions**

585 Figure 1: Upper inset: Location of Olympus Mons (OM) at the NW edge of the Tharsis Rise
586 (colour map and NW-SE general topographic profile from global MOLA DEM, vertical
587 exaggeration by a factor 17). Main Figure: Morphological characteristics of Olympus Mons from
588 MOLA data. (a) Shaded-relief map (illumination from top), (b) slope map, and (c) topographic
589 profiles (vertical exaggeration by a factor 9)

590

591 Figure 2: Morphological characteristics of Pico, Fogo, and Big Island. Upper panels: shaded-
592 relief maps (vertical illumination). Island coasts are drawn with thick black contours. The trace of
593 the main lateral flank failures is shown with dashed lines. Straight lines: trace of topographic
594 sections exposed in lower panels. Insets: location of the 3 islands on a cropped World map
595 (Lokal_Profil, Public Domain). PV: Pico Volcano; FV: Fogo Volcano; ML: Mauna Loa, MK:
596 Mauna Kea; K: Kilauea; HFS: Hilina Fault System. Lower panels: topographic cross-sections
597 (profile traces in upper panels).

598

599 Figure 3: (a) Fossil passage zone from sub-aerial to submarine lava flows on the island of Santa
600 Maria (Azores). Pl: pillow-lavas. (b) Close up on a pillow breccia in the submarine units at
601 present shore.

602

603 Figure 4: New model of evolution proposed for Olympus Mons. The inferred ages (in Ga) are
604 indicative. Vertical scale shows present elevation from MOLA data. The amount of subsidence
605 and surface uplift is derived from our new modelling of (1) lithosphere flexuration under early
606 volcanic load in the presence of an ocean (stages a and b) and inferred partial basin infill by

607 detrital sediments (grey colour) and (2) volcano uplift triggered by plume load and/or magma
608 underplating during emplacement of the Tharsis Rise (stage c) and/or late Amazonian activity
609 (stage d). See discussion in the main text.
610
611 Figure 5: Main morphological characteristics of Alba Mons from MOLA data. (a) Shaded-relief
612 map (illumination from W); (b) Topographic profiles from the centre to the outer parts of the
613 volcano (see profile traces in (a)).
614

Parameter	**Value**
E	100 GPa
ν	0.25
T_e	30, 50, 80, 100 and 150 km
ρ_c	3200 kg/m^3
ρ_m	3500 kg/m^3
ΔT plume	300 K
g	3.71 m/s^2

Hildenbrand et al., Table 1

Figure 1

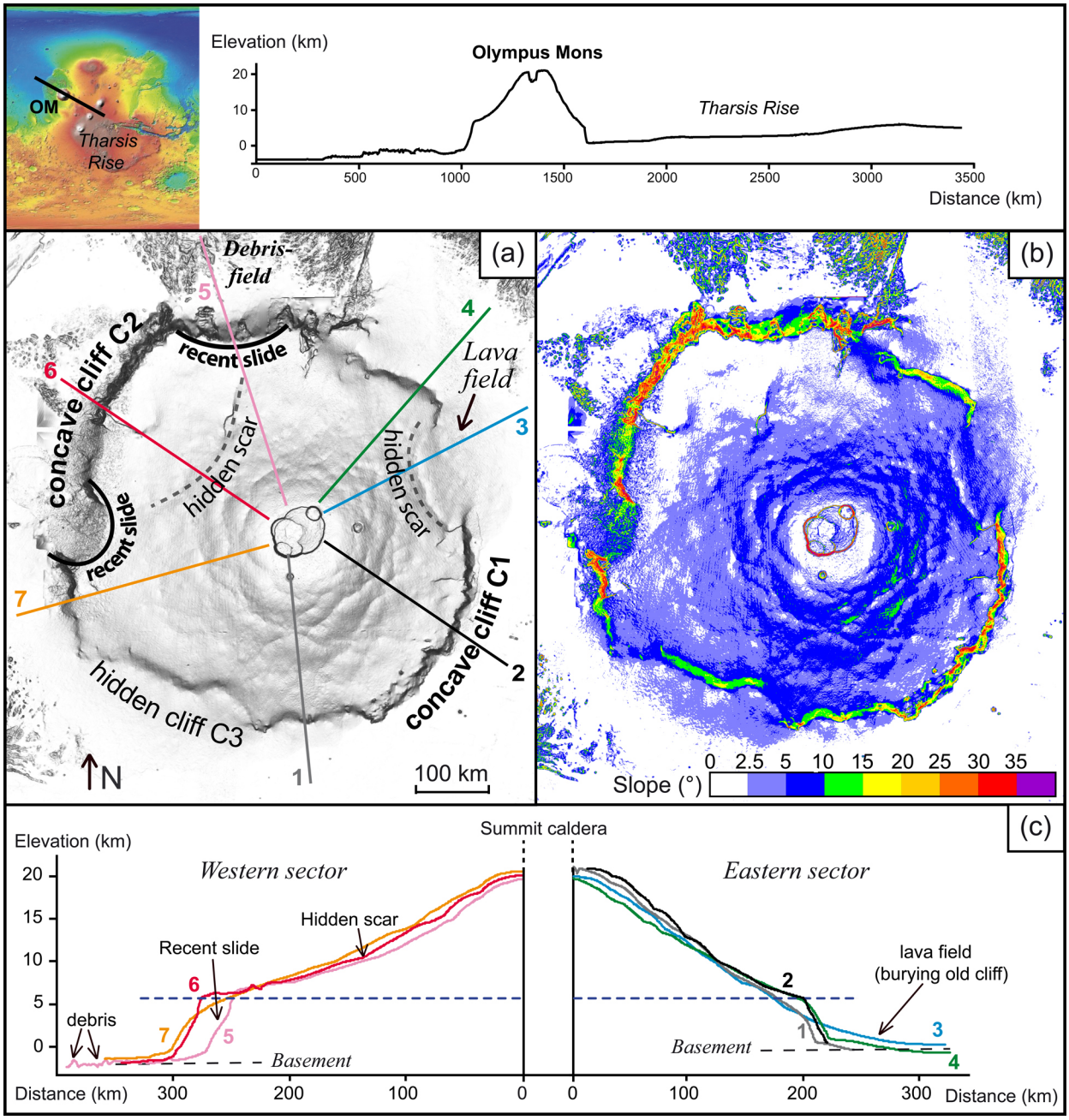
OM
Tharsis Rise
Elevation (km)
Olympus Mons
Tharsis Rise
Distance (km)
(a)
Debris-field
recent slide
concave cliff C2
hidden scar
Lava field
hidden scar
recent slide
concave cliff C1
hidden cliff C3
N
100 km
(b)
Slope (°)
(c)
Elevation (km)
Western sector
Summit caldera
Eastern sector
Hidden scar
Recent slide
debris
Basement
lava field (burying old cliff)
Basement
Distance (km)
Distance (km)

Figure 2

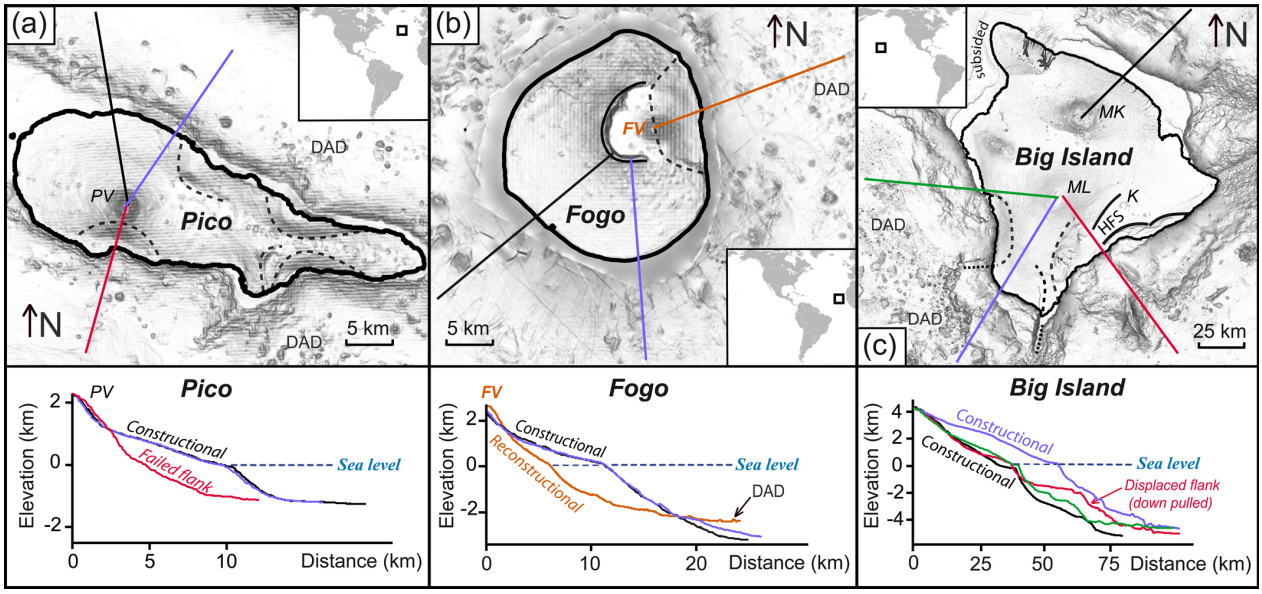

Figure 3

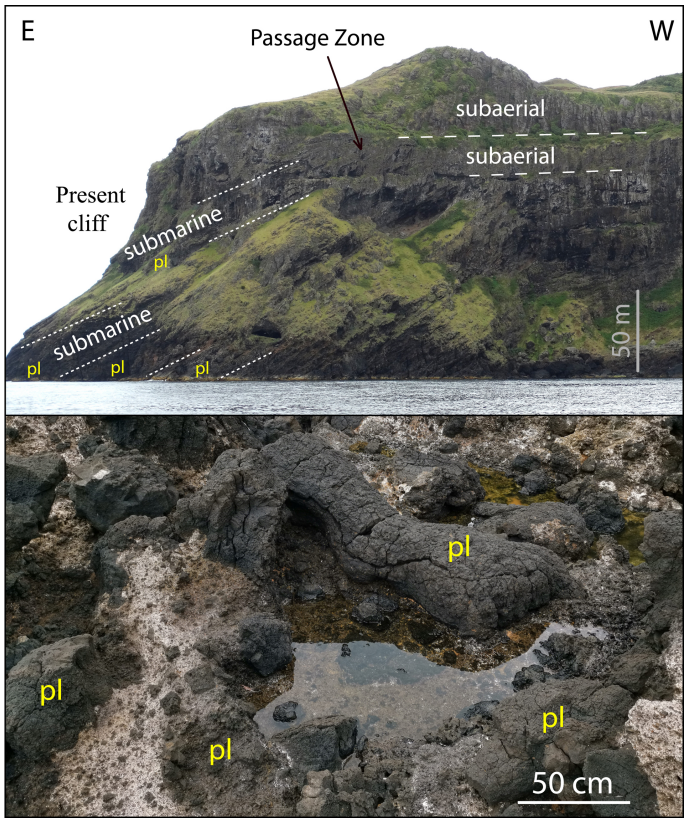

Figure 4

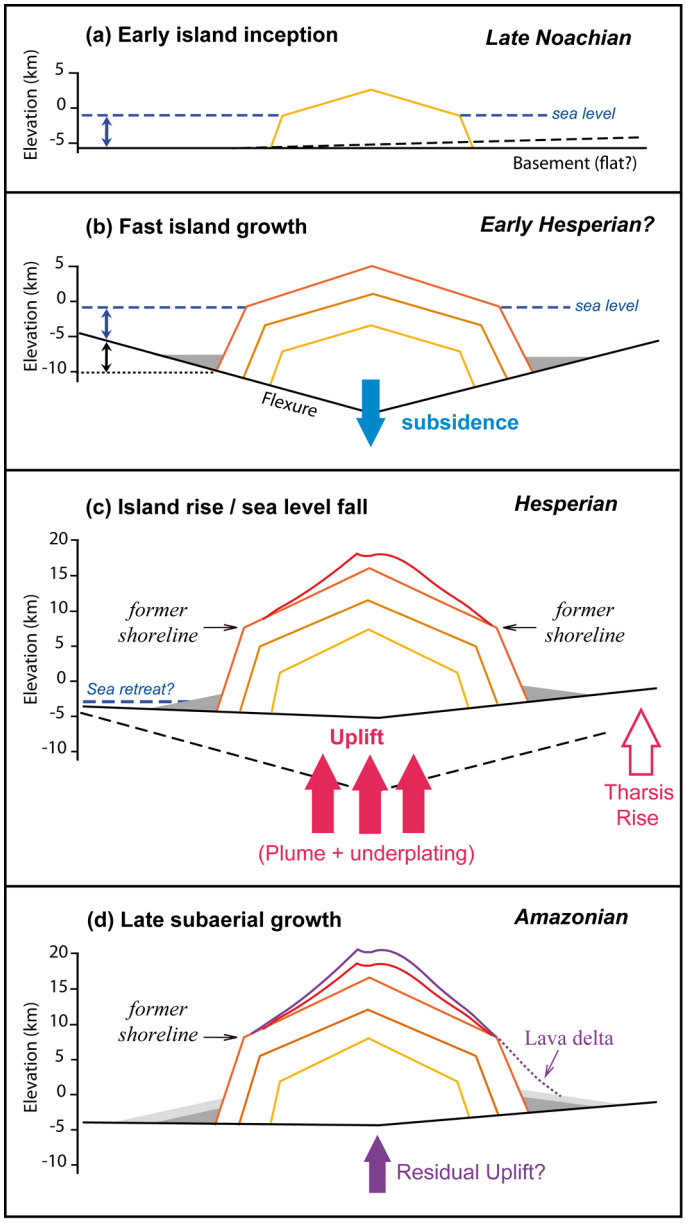
(a) Early island inception
Late Noachian
Elevation (km)
5
0
-5
sea level
Basement (flat?)
(b) Fast island growth
Early Hesperian?
Elevation (km)
5
0
-5
-10
sea level
Flexure
subsidence
(c) Island rise / sea level fall
Hesperian
Elevation (km)
20
15
10
5
0
-5
-10
former shoreline
former shoreline
Sea retreat?
Uplift
Tharsis Rise
(Plume + underplating)
(d) Late subaerial growth
Amazonian
Elevation (km)
20
15
10
5
0
-5
-10
former shoreline
Lava delta
Residual Uplift?

Figure 5

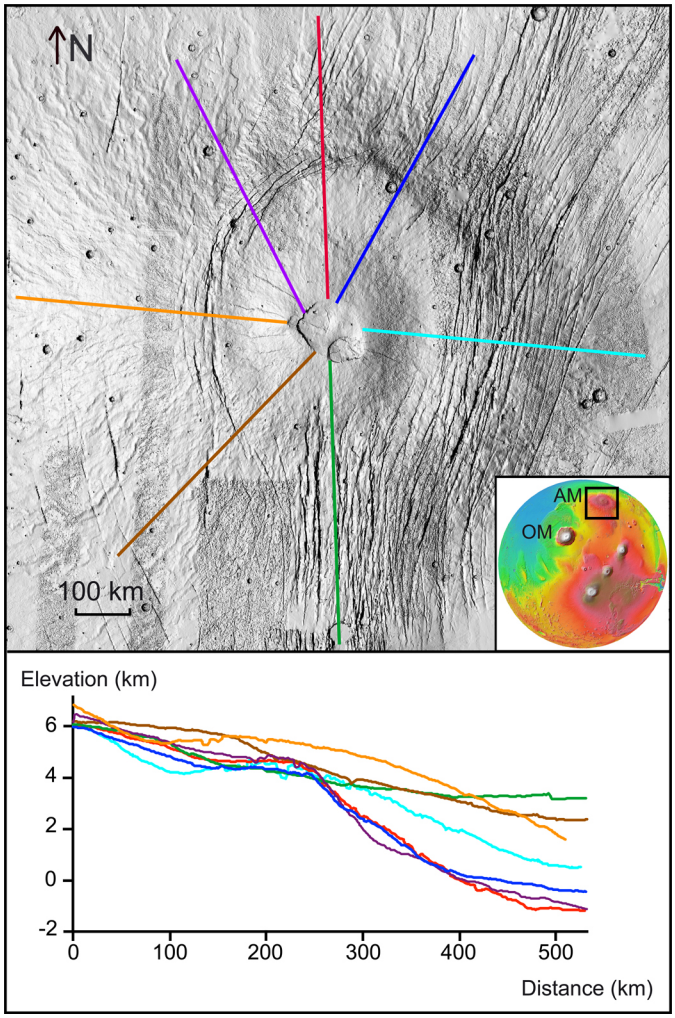
N
100 km
AM
OM
Elevation (km)
6
4
2
0
-2
0
100
200
300
400
500
Distance (km)